Multiscale modeling of capillary-driven contact line dynamics

Martin Kronbichler* Claudio Walker‡ Gunilla Kreiss*
Bernhard Müller‡

Abstract

We present a multiscale method to simulate the flow of two immiscible incompressible fluids in contact with solids. The macro model in our method is based on a level set method with sharp interface treatment. The contact line is tracked explicitly and moves according to a slip velocity that depends on the apparent contact angle of the interface with the solid. The relation between apparent contact angle and slip velocity is determined in a micro model based on the phase field method. The phase field method seeks for an equilibrium slip velocity in a box around the contact point, given a static contact angle at the solid and the apparent contact angle in the far field. The dimensions of the box are chosen in the range of physical diffusion length scales at the contact point. We present numerical results of the multiscale method for capillary-driven flows which demonstrate the convergence of results in the macro model and compare the behavior with other approaches in contact line dynamics.

Key words. Capillary-driven flow, contact line dynamics, phase field method, level set method, ghost fluid method.

1 Introduction

The numerical simulation of incompressible fluid flow with several immiscible fluids is very challenging, both from a methodological and an implementation point of view. A major challenge is the prediction of the physical behavior when the interface that separates two fluids is in contact with a solid and moves, a so-called moving contact line. Applications where the contact line behavior is significant can be found in micro fluidics, coating processes, and biological flows.

The standard model for two-phase flow consists of the incompressible Navier–Stokes equations, combined with a mechanism to transport the interface with the local fluid velocity. This model cannot be combined with conventional no-slip boundary conditions at solids because this would lead to a singularity in the stresses around

*Division of Scientific Computing, Department of Information Technology, Uppsala University, Box 337, 751 05 Uppsala, Sweden (martin.kronbichler@it.uu.se, gunilla.kreiss@it.uu.se).

‡Department of Energy and Process Engineering, Norwegian University of Science and Technology, Kolbjørn Hejes vei 2, 7491 Trondheim, Norway (claudio.walker@ntnu.no, bernhard.muller@ntnu.no).

the contact line [24]. The singularity in the model can be avoided if the contact line is allowed to slip [23]. A common choice is the so-called Navier condition, which relates the slip velocity $\mathbf{u}_{\text{slip}}$ along the wall to the shear stress,

$$\mathbf{u}_{\text{slip}} = \lambda \mathbf{n} \cdot \left(\nabla \mathbf{u} + (\nabla \mathbf{u})^T \right), \tag{1}$$

where λ is the so-called slip length parameter, see [5, 41]. The Navier condition is sufficient for flows that are driven by external forces. For capillary-driven flows, on the other hand, the contact angle between the interface and the solid must also be taken into account. In numerical algorithms based on the level set method [39] or the volume of fluid method [22], the contact angle is often implemented through a manipulation of the level set function or the volume fraction, respectively [36, 28, 43]. For the simulation of dynamic contact lines, the contact angle can either be arbitrarily fixed for the whole simulation time [4], be based on a time series obtained from experiments [16], or dependent on the fluid velocity close to the contact line [41]. Spelt [41] proposed to track the contact point explicitly and set its velocity as a function of the contact angle. Another possibility is to move the contact point through diffusion like in the phase field method presented below.

An alternative approach to overcome the singularity at the contact line is the application of multiscale models. The idea is to represent the bulk of the domain with a conventional continuum model and couple it to a more detailed (molecular) model around the contact line. The first multiscale approach to two-phase flows was proposed by Hadjiconstantinou [17]. To couple the molecular dynamics to the continuum description, the domains of the two models overlap. In each time step, several iterations are computed on each domain using the results of the other model as boundary conditions in the overlapping region until the two models converge in the shared region. A more generic approach to couple models based on different physical descriptions at different scales is the heterogeneous multiscale method [8, 9], which relies on a solid mathematical theory. This method was successfully applied to two-phase flow [33]. The micro model is usually based on molecular dynamics as in the approach by Qian and co-workers [30, 31], see also the review paper [32]. For a discussion of different models for contact line dynamics, we refer to [34, 35] and references therein. All the aforementioned approaches of multiscale models have been applied to two immiscible fluids in Couette or Poisseuille flows with equal fluid densities and viscosities.

In this work, we propose a continuum model based on the Cahn–Hilliard/Navier–Stokes equations as a micro scale description. Our approach enables accurate contact dynamics also for more complex flows with variable densities and viscosities, compared to methods relying on molecular dynamics. In a micro model, we determine the slip velocity for a given apparent contact angle. This relation is applied as a boundary condition in the macro model. The information of the micro model can be pre-computed and tabulated prior to the macro simulation, which makes the actual simulation costs of the macro model similar to previous approaches based on ad-hoc relations like the method by Spelt [41]. Standard numerical techniques are possible for the implementation of the macro solver. For demonstration, we choose a level set discretization with sharp interface treatment using the ghost fluid method. The two crucial aspects in the macro solver are to find accurate values for the curvature at the contact point and to impose the slip boundary condition around the contact point in a suitable way.

Our approach requires both a spatial and temporal scale separation between the local contact line behavior and global fluid flow. Since we consider flows which are driven by capillary forces, the assumption that the flow on the micro scale is reacting much faster than the flow on the macroscale is justified. This temporal scale separation implies that the micro problem is in equilibrium for each apparent contact angle and therefore no additional information from the macro model is required. Simulation of more complicated flows that e.g. include surfactants would require additional data exchange.

The accuracy of our multiscale approach depends on the quality of the micro results. We assume that the phase field method gives a sufficiently accurate representation of the physics at the contact line, in case the actual physical values of diffusion length scale and diffuse interface width in the Cahn–Hilliard equation are well-resolved. In global phase field simulations, resolution aspects of the numerical implementation often limit the choice of these parameters, with physically meaningful values out of reach. Hence, there is a notable uncertainty in phase field results for many important applications, also when employing state-of-the-art numerical techniques like adaptive mesh refinement and higher order schemes. The study of contact line behavior by Yue et al. [42] revealed the importance of the diffusion length scale as the relevant parameter in phase field representations, and identified convergence with respect to the diffuse interface width. Our approach avoids parameters dictated by the numerics, resulting in micro simulations which are performed at physically meaningful diffusion length scale and diffuse interface width, respectively.

The outline of this article is as follows. In the following section, we outline the phase field method that constitutes the micro model and describe the algorithm that is used to determine the slip velocity. We analyze the behavior of the micro solver with respect to mesh resolution and diffuse interface width. In Sec. 3, we introduce a macro solver based on the level set method and discuss the numerical aspects of determining contact angle and prescribing motion at the contact point. In Sec. 4, computational results for several test problems relevant to capillary-driven flow are presented. Finally, Sec. 5 summarizes the findings.

2 Micro model

In this section, we describe the micro model that is used to compute a relation between the apparent contact angle and the slip velocity. The apparent contact angle is the angle between the interface and the solid measured in the macro simulation at a given instant in time. The slip velocity only depends on the apparent contact angle. It is therefore most efficient to perform the micro simulation independently of the macro simulation, and tabulate the results for use in the macro model.

2.1 Phase field method

The phase field method for a system of two immiscible incompressible fluids is based on a mathematical model consisting of the coupled Cahn–Hilliard/Navier–Stokes equa-

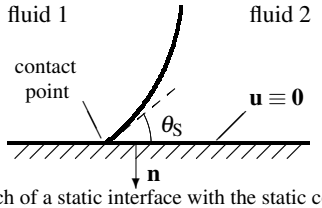

Figure 1: Sketch of a static interface with the static contact angle θ_S.

tions posed on a single domain Ω,

$$\frac{\partial c}{\partial t} + \mathbf{u} \cdot \nabla c - m\nabla^2 \psi = 0, \tag{2}$$

$$\psi - \frac{3\sigma\varepsilon}{4}\left(\frac{2}{\varepsilon^2}(c^3 - c) + \nabla^2 c\right) = 0, \tag{3}$$

$$\nabla \cdot \mathbf{u} = 0, \tag{4}$$

$$\rho\left(\frac{\partial \mathbf{u}}{\partial t} + \mathbf{u} \cdot \nabla \mathbf{u}\right) - \nabla \cdot (2\mu \nabla^s \mathbf{u}) + \nabla p = \psi \nabla c + \rho \mathbf{g}, \tag{5}$$

where c is a concentration or order parameter that is $+1$ and -1 in either fluid with a smooth transition in between. The variable $\psi = \psi(c)$ denotes the chemical potential, and the term $c^3 - c$ represents a double-well potential. The Cahn–Hilliard equation (2)–(3) is derived from an interfacial free energy [3, 26]. The term $\mathbf{u} \cdot \nabla c$ accounts for convective transport by the fluid velocity $\mathbf{u}$. The variable p denotes the fluid pressure, and $\nabla^s \mathbf{u} = \frac{1}{2}(\nabla \mathbf{u} + (\nabla \mathbf{u})^T)$ is the rate of strain tensor. The parameters $\rho = \rho_1 + \frac{1}{2}(\rho_2 - \rho_1)(1-c)$ and $\mu = \mu_1 + \frac{1}{2}(\mu_2 - \mu_1)(1-c)$ represent density and dynamic viscosity, m represents mobility, σ surface tension, and ε controls the diffuse interface width. For a plane interface with normal parallel to the x-direction, the interface profile is given by $\tanh(x/\varepsilon)$. Our notation can be converted to the notation used in [25, 26] with $\psi = \beta\left(c^3 - c\right) - \alpha\nabla^2 c$ and parameters $\alpha = 3\sigma\varepsilon/2$ and $\beta = 3\sigma/4\varepsilon$. The gravitational acceleration vector is given by $\mathbf{g}$. Note that the Cahn–Hilliard equation (2)–(3) is written as a system, which is the form used in the numerical implementation in Sec. 2.4 below. The term $\psi\nabla c$ in the momentum equation represents surface tension.

Boundary conditions supplement the above equations. On a solid boundary according to Fig. 1, these conditions are

$$\mathbf{u} = \mathbf{0}, \tag{6}$$

$$\mathbf{n} \cdot \nabla \psi = 0, \tag{7}$$

$$\mathbf{n} \cdot \nabla c + \cos(\theta_S)(1 - c^2) = 0, \tag{8}$$

where $\mathbf{n}$ denotes the unit normal vector on the boundary and θ_S denotes the static contact angle between the fluid-fluid interface and the solid, see [26]. The static contact angle is defined as the angle at which no forces originate from the contact point, and is in general different from a dynamic contact angle observed for moving interfaces.

2.2 Physics of the micro model

The phase field method allows for contact line motion despite no-slip boundary conditions through diffusive mass transfer around the contact line [38, 26]. In the micro

model, we use this effect to find a balance between the diffusion and a relative velocity of the wall, the so-called slip velocity. The phase field solution is characterized by two inherent length scales [26, 42]. The first length scale is the diffuse interface width ε. The mobility m gives rise to the second length scale, the range over which diffusive transport is active. In terms of the solution to the Cahn–Hilliard equation, there is a jump in c from $+1$ to -1 over a range proportional to ε, and the chemical potential is non-trivial in a region of size proportional to m. Hence, also interface forces are concentrated to a region whose size is determined by ε and m.

We base the micro simulation on physical values for ε and m for the fluids under consideration. Typical length scales are a few tens to hundreds of nanometers [26, 2]. An interface on a macroscopic scale exhibits radii of curvature that are usually much larger than the relevant region for the micro-scale simulation. In other words, the interface is essentially plane at length scales relevant to diffusive transport. This implies that the solution on the micro scale is approximately two-dimensional around the interface and it suffices to solve the micro problem in two spatial dimensions.

At nanometer length scales, the ratio between viscous and inertial forces in the Navier–Stokes equations is very high, i.e., the Reynolds number is very low, $\mathrm{Re} \ll 1$. Consider e.g. the flow at a length scale of 20 nm and a velocity of $100\,\mathrm{mm/s}$ for water with a dynamic viscosity $\mu = 8.9 \cdot 10^{-4}\,\mathrm{Pa\,s}$. Then, the Reynolds number is $2.2 \cdot 10^{-3}$. Hence, we can neglect all inertial and gravitational effects in the micro model. In this setting, the Navier–Stokes equations reduce to the Stokes equations with continuity equation (4) and momentum equation given by

$$-\nabla \cdot (2\mu \nabla^{\mathrm{s}} \mathbf{u}) + \nabla p = \psi \nabla c. \tag{9}$$

In our micro model, the Stokes system is coupled to the Cahn–Hilliard equation (2)–(3), and it is time-dependent due to this coupling.

As a computational domain, we choose a box of height L, which needs to be chosen large enough in order to fully represent the diffusion region in the Cahn–Hilliard equation. The length of the box is selected to cover the complete interface (including some additional space in order to allow the contact position to develop), and varies with the apparent angle θ_{a}. Fig. 2 depicts the computational domain together with the boundary conditions defined in Sec. 2.3 below. The flow in the micro model is characterized by the following non-dimensional numbers:

$$\begin{aligned} \mu^* &= \frac{\mu_1}{\mu_2} && \text{(viscosity ratio)}, \\ S &= \frac{\sqrt{m\mu_1}}{L} && \text{(diffusion length)}, \\ \mathrm{Cn} &= \frac{\varepsilon}{L} && \text{(Cahn number)}, \end{aligned}$$

where μ_1, μ_2 are the dynamic viscosities of fluid 1 and 2, respectively. Together with the static contact angle, these physical parameters fully describe the Cahn–Hilliard/ Stokes system. As opposed to e.g. the approach taken by Spelt [41], no additional parameters dictated by numerics need to be introduced.

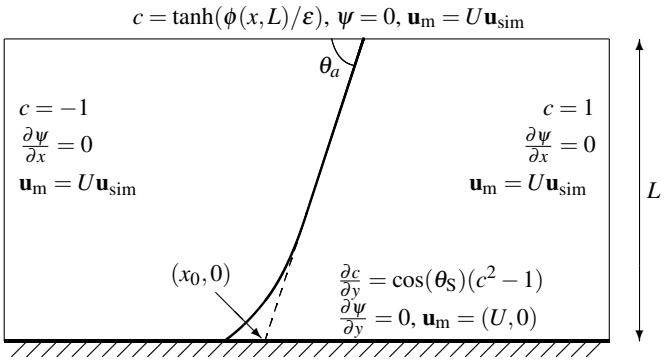

Figure 2: Schematic illustration of micro model with boundary conditions. The similarity velocity $\mathbf{u}_\mathrm{sim}$ is centered at the point $(x_0, 0)$, the extension of a plane interface to the boundary.

2.3 Boundary conditions for the micro model

Since the velocity field does not decay away from the contact point, we need to define the behavior of the velocity at the boundary of the box in the micro model. The flow around a plane interface at zero Reynolds numbers can be approximately described by the creeping flow model introduced by Huh and Scriven [24]. The Huh–Scriven model gives a similarity solution for the velocity $\mathbf{u}_\mathrm{sim}$ based on the contact angle θ_a and the viscosity ratio μ^*. Of course, the creeping flow model breaks down close to the contact point because of the singularity in the shear stress. For our micro model, the similarity velocity $\mathbf{u}_\mathrm{sim}$ is expanded around the point $(x,y) = (x_0, 0)$, the extension of a plane interface to the wall, see Fig. 2, and we only assume the similarity solution to hold in the far field, namely at the boundary of the micro domain. In our simulation, the inherent diffusion of the phase field method avoids the stress singularity. Note that the similarity velocity is not related to the interface description by the phase field method, and does not specify values for the variables c and ψ.

As explained above, the purpose of the micro model is to find a slip velocity U given a certain apparent contact angle θ_a from the flow field in a small domain around the contact point. The slip velocity U describes the relative motion of the contact point which is in balance with the diffusion in the phase field method, given the apparent contact angle. The similarity velocity expressed in terms of an interface velocity equal to unity is related to the slip velocity by scaling it by the slip magnitude U. In order to restrict the simulation to a fixed domain, we let the simulation domain follow the contact point speed U by changing the frame of reference.

The following boundary conditions are set in the micro simulation, compare with Fig. 2:

- Along the solid wall, we assume the usual phase field boundary condition (7)–(8) together with a convectional no-slip boundary condition (6) for the velocity. Due to the change of frame of reference, the boundary condition is $\mathbf{u}_\mathrm{m}\big|_\mathrm{wall} = (U, 0)$.
- The velocity field on the open boundaries is set according to the Huh–Scriven similarity velocity [24], scaled by the slip velocity, $\mathbf{u}_\mathrm{m}\big|_\mathrm{open} = U\mathbf{u}_\mathrm{sim}$.

- The concentration variable along the upper boundary follows the profile that is attained by plane interfaces, $c(\mathbf{x}) = \tanh(\phi(\mathbf{x})/\varepsilon)$, where $\phi(\mathbf{x})$ denotes the signed distance of $\mathbf{x}$ from the initial interface. This makes sure that the interface does not move along the upper boundary. At the left and right boundaries, c is set to -1 and $+1$, respectively. The chemical potential is set to a homogeneous Dirichlet-type condition at the upper boundary and no-flux (7) at the left and right boundaries, respectively. These conditions ensure the contribution from surface tensions is zero at the open boundaries, as expected for a straight interface.
- Since Dirichlet conditions for the velocity are imposed on the whole boundary of the domain, the pressure is only determined up to a constant. We fix the pressure in the lower left corner of the domain to zero.

The simulation is started with a plane interface aligned with the apparent contact angle, see Fig. 2, i.e., $c(\mathbf{x}) = \tanh(\phi(\mathbf{x})/\varepsilon)$. Note that the apparent contact angle θ_a is not enforced as boundary condition in the micro simulation. However, as the result of the micro simulation, a steady state will be found for the given initial position described by θ_a.

2.4 Numerical implementation of phase field solver

For convenience of implementation, we solve the micro model for a velocity variable $\mathbf{u}$ that satisfies zero Dirichlet conditions along the whole boundary also in the moving frame of reference,

$$\mathbf{u} = \mathbf{u}_\mathrm{m} - U\mathbf{u}_\mathrm{sim}, \tag{10}$$

where $\mathbf{u}_\mathrm{m}$ is the velocity, and $U\mathbf{u}_\mathrm{sim}$ is the similarity velocity. This introduces additional forcing due to viscous dissipation of the similarity velocity.

We discretize the system (2)–(4)&(9) with the finite element method. To this end, we first write the system in weak form, where the objective is to find functions $\mathbf{u}, p, c, \psi$ in suitable Sobolev spaces (weak first derivatives, boundary conditions according to Sec. 2.3) such that

$$\begin{aligned}
\left(v_c, \frac{\partial c}{\partial t} + (\mathbf{u} + U\mathbf{u}_\mathrm{sim})\cdot\nabla c\right)_\Omega + \left(\nabla v_c, S^2\nabla\psi\right)_\Omega &= 0,\\
\left(v_\psi, \psi - \frac{3(c^3-c)}{2\,\mathrm{Cn}}\right)_\Omega - \frac{3\,\mathrm{Cn}}{4}\left(\left(\nabla v_\psi, \nabla c\right)_\Omega + \left(v_\psi, \cos(\theta_\mathrm{S})(1-c^2)\right)_{\Gamma_\mathrm{wall}}\right) &= 0,\\
(v_p, \nabla\cdot\mathbf{u})_\Omega &= 0,\\
(\nabla^\mathrm{s}\mathbf{v}_u, 2\nu\nabla^\mathrm{s}\mathbf{u})_\Omega + U\,(\nabla^\mathrm{s}\mathbf{v}_u, 2\nu\nabla^\mathrm{s}\mathbf{u}_\mathrm{sim})_\Omega - (\nabla\cdot\mathbf{v}_u, p)_\Omega - (\mathbf{v}_u, \psi\nabla c)_\Omega &= 0,
\end{aligned} \tag{11}$$

holds for all admissible test functions $v_c, v_\psi, v_p, \mathbf{v}_u$. We define a smoothly varying non-dimensional viscosity as $\nu = (1-c) + \mu^*(1+c)$, where μ^* denotes the viscosity ratio, see Sec. 2.2. For discretization, the domain is subdivided into rectangular elements and the infinite-dimensional spaces are approximated by piecewise polynomial approximations on the elements. For the Cahn–Hilliard variables c and ψ, bi-linear basis functions Q_1 on the elements are chosen. For the Stokes system, bi-quadratic $\mathscr{Q}_2^d$ elements for velocity and Q_1 elements for pressure are chosen, which satisfy the so-

called inf–sup condition, see e.g. [14], and thus give a stable discretization. Equation (11) is then enforced on the finite-dimensional subspaces.

The time derivative is approximated using BDF-2 [18], i.e., $\partial c^{n+1}/\partial t \approx (3c^{(n+1)} - 4c^{(n)} + c^{(n-1)})/(2\Delta t)$ and the other terms are evaluated at time level $n+1$. The nonlinear term c^3 in the chemical potential equation is approximated by a linearly stabilized splitting similar to the one described in [11],

$$(c^3 - c)^{(n+1)} \approx 2(c^3 - 3c)^{(n)} - (c^3 - 3c)^{(n-1)} + 2c^{(n+1)}.$$

The idea of the splitting is to choose a quadratic envelope function c^2 for the double-well potential $\frac{1}{4}(c+1)^2(c-1)^2$, based on the interpretation of the Cahn–Hilliard equation as a gradient system. Likewise, the nonlinearity in the boundary term is approximated by the splitting

$$(1 - c^2)^{(n+1)} \approx 2(1 + 2s_\theta c - c^2)^{(n)} - (1 + 2s_\theta c - c^2)^{(n-1)} + 2s_\theta c^{(n+1)},$$

where $s_\theta = \text{sign}(\cos(\theta))$.

The coupling between the momentum equation and Cahn–Hilliard equation is resolved by an explicit segregation approach. In one time step, we first solve for the Cahn–Hilliard equation with a velocity extrapolated to the new time level, $\mathbf{u}^* = 2\mathbf{u}^{(n)} - \mathbf{u}^{(n-1)}$, and then the Stokes equation with new values for $c^{(n+1)}$ and $\psi^{(n+1)}$. This avoids nonlinear iterations during one time step, but introduces a limit on the time step $\Delta t \sim \frac{\mu}{\sigma}\Delta x$, see [13].

After space and time discretization, we obtain two linear systems to be solved, one for the Cahn–Hilliard system and one for the Stokes system. For the former, we choose the sparse direct solver UMFPACK [6], and for the latter we use a generalized minimum residual solver (GMRES) with Schur complement preconditioner based on a pressure mass matrix, as discussed in [10]. The phase field solver is implemented in C++ based on the finite element library deal.II [1].

2.5 Material parameters for a water/oil micro model

In order to exemplify the numerical algorithm, we provide computational results for water and oil in the next subsection. Of course, the algorithm is generic and applies to any combination of two immiscible fluids. The material parameters of our sample problem are given in Table 1. The table also indicates the mesh resolution and time step size used in the experiments throughout this section. We use non-dimensional quantities in the simulation. Since there are no inertial terms, only surface tension and viscous forces appear. Therefore, we scale the equations so that the non-dimensional coefficient for surface tension (capillary number) is one. For the actual problem, the velocity is obtained through the relation $U_{\text{dim}} = U\frac{\sigma}{\mu}$, where U is the non-dimensional velocity determined by the micro model. Note that the Cahn number is within the range $\text{Cn} \leq 4S$ identified in [42] for convergence at contact lines.

2.6 Computation of slip velocity

The algorithm outlined in Sec. 2.4 simulates the time-dependent dynamics of two-phase flow for given material parameters and boundary conditions. In our case, we

Table 1: Parameters for the oil-water case. Note that only the given non-dimensional numbers are used in the computations. The static contact angle is measured from the oil side, i.e., water is wetting.

ρ_1 $\left[\frac{\text{kg}}{\text{m}^3}\right]$	ρ_2 $\left[\frac{\text{kg}}{\text{m}^3}\right]$	μ_1 $\left[\frac{\text{kg}}{\text{m s}}\right]$	μ_2 $\left[\frac{\text{kg}}{\text{m s}}\right]$	σ $\left[\frac{\text{kg}}{\text{s}^2}\right]$	μ^* –	Cn –	S –	θ_S [degrees]	Δx –	Δt –
1000	730	0.001	0.00334	0.054	3.34	0.06	0.0316	140	$\frac{1}{64}$	0.001

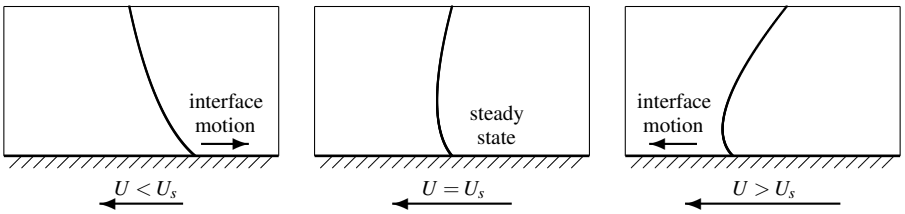

Figure 3: Schematic illustration of reaction to different wall velocities. If the wall velocity U is too low or too high, the interface moves to either right or left.We denote the velocity for which steady state is reached by U_s. Fig. 4 shows computational results for this situation. The static contact angle θ_S is assumed to be 140 degrees and the apparent contact angle θ_a equals 80 degrees in this illustration.

have to find a boundary velocity U for which the phase field simulation reaches a steady state. This is a problem of inverse type [21, Chapt. 1].

Since the inverse problem to be solved has a one-dimensional input variable (apparent contact angle θ_a, which in turn defines $\mathbf{u}_{\text{sim}}$ and the initial location of the interface $c(\cdot, t=0)$), and has a one-dimensional output U, we choose the secant method for solving $f(U)=0$. The task is to define a function f that gives zero for a slip velocity U that yields steady state in the phase field simulation, and a positive or negative reaction when the velocity is too small or too high, respectively. A candidate function is based on the behavior of the contact point: As displayed in Fig. 3, the contact point position of the interface with the wall moves to the rightwhen the wall velocity is too low, and to the leftif the wall velocity is too high. Fig. 4 shows actual simulation results for the shape of the interface as well as the velocity field. The steady state solution is based on the result with the secant method described below.

Figs. 5 and 6 illustrate the behavior of the phase field solution with time for two different apparent contact angles and the water-oil material combination. Fig. 5 shows the behavior at an apparent contact angle equal to the static contact angle, where a zero slip velocity should ideally give steady state. We observe that the long-time behavior of zero velocity is not a complete steady state (see solid red line) because of discretization errors. However, as expected, a positive velocity gives a deviation to the right, and a negative velocity a deviation to the left. Fig. 6 shows the location of the contact point over time for an apparent contact angle of 80 degrees, both in linear and logarithmic time scale. For this case, a non-zero slip velocity is needed to stabilize the system. The reaction is studied for several values of the velocity. The solid red line shows the time evolution for the numerically computed slip velocity that yields a steady state, together with two slip velocities that are too small (contact point drifts to the left) and two where the slip velocities are too large (contact point drifts to the right).

The results in Figs. 5 and 6 indicate that the measured speed of the contact point is a good candidate for defining $f(U)$. Other one-dimensional quantities that take up

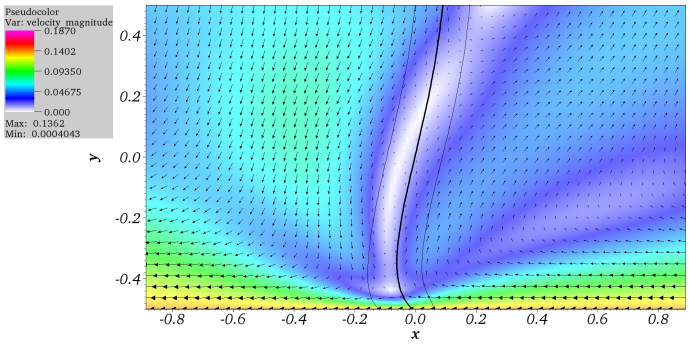

(a) Slip velocity that gives steady state with the secant algorithm in Sec. 2.7.

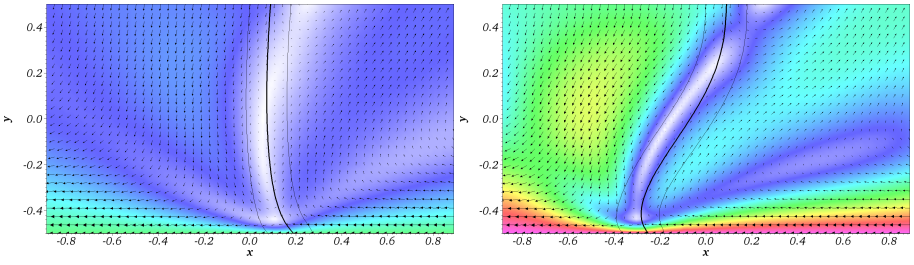

(b) Slip velocity too low.

(c) Slip velocity too high.

Figure 4: Velocity field for phase field simulations with three different slip velocities U. The static contact angle is 140 degrees, and the apparent angle is 80 degrees. The interface is indicated by a thick solid line, and the two thin lines give the location of the -0.9 and $+0.9$ contour lines in the concentration c. The color displays the magnitude of the total velocity field $\mathbf{u}_{\mathrm{m}} = \mathbf{u} + U\mathbf{u}_{\mathrm{sim}}$.

the motion of the interface based on the concentration variable c are also possible. We emphasize that the steady state found by our algorithm does not depend on the particular choice of the function $f(U)$, as long as there is a distinct zero value. In Fig. 7, we study the properties of the function f chosen to be the actual contact point velocity for an apparent contact angle of 80 degrees. We see that there is a clear zero value, which enables the use of standard techniques to find zeros.

Since system (11) is time-dependent, we need to identify a suitable time for when to record $f(U)$. As can be seen from Fig. 6(a), an initial transient is present in the system where the interface changes from the apparent contact angle towards the prescribed static contact angle. From non-dimensional time $t \approx 5$ onwards, an approximately linear behavior of the contact point position develops. Therefore, it is reasonable to measure the contact point speed during this phase. We choose the final time for the micro simulation to be 10 times the time interval of initial transients, i.e., time 50, for evaluating $f(U)$.

2.7 Secant method

The problem of finding the slip velocity given an apparent contact angle has now been reduced to solve the one-dimensional non-linear equation

$$f(U) = 0, \tag{12}$$

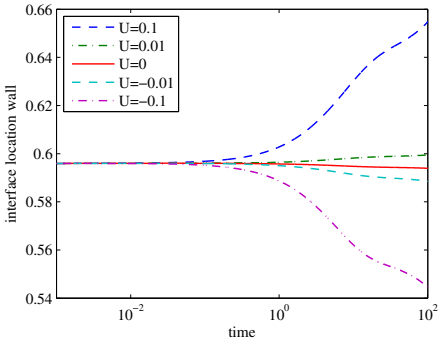

Figure 5: Time evolution of the position of the interface at the wall boundary in a logarithmic scaling of time. The materials considered are water and oil with static contact angle equal to 140 degrees (measured from the oil side), and the apparent contact angle equals the static contact angle.

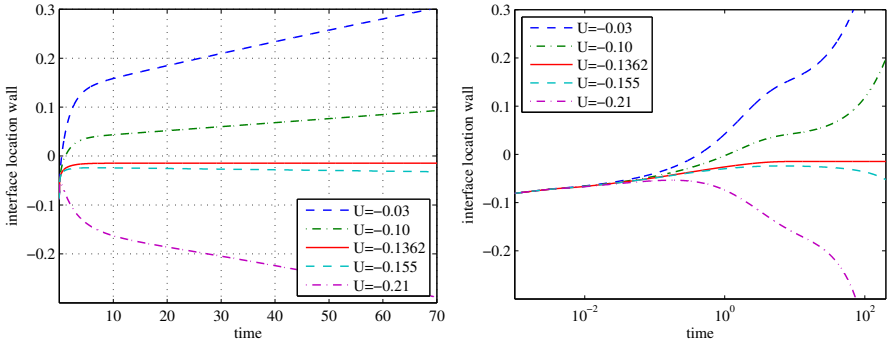

(a) Linear time scale. (b) Logarithmic time scale.

Figure 6: Time evolution of the position of the interface at the wall boundary. The materials considered are water and oil with static contact angle equal to 140 degrees (measured from the oil side), and the apparent contact angle is equal to 80 degrees. The velocity $U = -0.1362$ is the solution from the secant method (13).

where f is the measured velocity of the contact point motion. For the solution of equation (12), we use the secant method. We choose an initial velocity U_0 (as result from a simulation with slightly different material parameters, result from a simulation at a neighboring apparent contact angle, or simply zero), and a perturbed velocity, e.g. $U_1 = U_0 + 0.01$. The iteration to find the next velocity is then

$$U_{k+1} = U_k - f(U_k)\frac{U_k - U_{k-1}}{f(U_k) - f(U_{k-1})}, \quad k = 1, 2, \ldots \tag{13}$$

We stop the iteration as soon as the update $U_{k+1} - U_k$ is smaller than a given tolerance, say 10^{-5}. Since we solve the Stokes linear system only approximately with an iterative method, the function value $f(U)$ contains a certain degree of noise, which might affect the secant method. We found that solving the Stokes systems to an absolute residual about two orders of magnitude smaller than the secant method tolerance eliminated this influence. In all the experiments we conducted, the secant method converged in three to seven steps, which means that not more than eight function evaluations $f(U_k)$

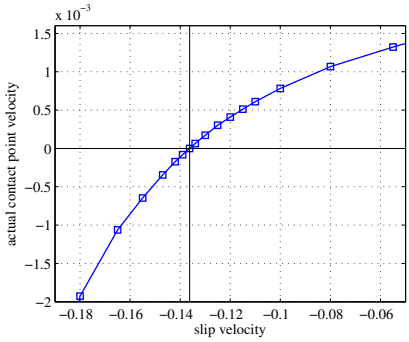

Figure 7: Actual contact point velocity for water and oil at an apparent contact angle of 80 degrees for different values of the slip velocity measured at time 50. The secant algorithm in (13) searches the zero of this function, which is around -0.1362 in this case.

were necessary to find the correct slip velocity. These good convergence properties are due to the clear zero position in $f(U)$, see Fig. 7.

Another approach to solve the inverse problem stated above would be to cast the problem as an optimization problem with PDE constraints, see e.g. [21]. The control variable is then the velocity U, and the target function is some suitable measure for steady state based on the rate of change in the concentration variable. The solution of such a problem usually involves performing a sequence of forward and backward evaluations based on the time-dependent PDE model (11), where the control variable U is systematically varied in order to approach the steady state. To the best of our knowledge, it is not possible to infer the steady-state of the time-dependent phase field method (11) from the solution of a stationary problem, which makes the overall cost for solving the time-dependent inverse problem at least as expensive as the secant method.

2.8 Tabulation of micro results

In order to use the micro model for simulations, its information needs to be integrated into a macro simulator. There are two possibilities to do this. One way would be to measure the angle in the macro model in each time step and then find U on the fly. This is, however, very expensive since it involves solving several time-dependent PDE problems in order to find the correct slip velocity, even when starting with good initial guesses. A second possibility is to pre-compute the slip velocity for a wide range of apparent contact angles and to collect the results in a table as $F(\theta_{\mathrm{a}}^k), k = 1,\ldots,N$. From the table, one can compute $F(\theta)$ for an arbitrary θ by interpolation. We chose this approach and performed 30 simulations for angles between 40 and 160 degrees. The resulting graph for water and oil is shown in Fig. 8.

2.9 Convergence behavior of micro model

The micro model is based on physical assumptions regarding the length scales of diffusion around the contact point. In order to obtain accurate results for the slip velocity U, we need to ensure that the discretization resolves the physical features

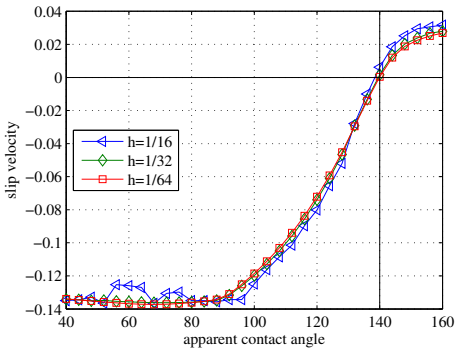

Figure 8: Wall velocities for water and oil material combination at different mesh sizes. For $h = 1/16$ and $h = 1/32$, the time step size is 0.0025, and for $h = 1/64$ it is 0.001.

of the flow, and that the diffusion along the contact point is captured by the diffuse Cahn–Hilliard interface, as explained in Yue et al. [42]. In Fig. 8, we consider the results $F(\theta^k)$ for three different mesh sizes and appropriate time steps. The Cahn number is fixed at $\mathrm{Cn} = 0.06$ and the diffusion length $S = 0.0316$. For the coarsest mesh considered, $h = \frac{1}{16}$, the interface is not completely resolved because $h \approx \mathrm{Cn}$ and thus the results are a bit irregular. However, the agreement to finer mesh sizes is still very good. The results from $h = \frac{1}{32}$ and $\frac{1}{64}$ are in close agreement (relative difference between 1 and 2 percent), which shows that the numerical solution is well-converged for the given parameters Cn and S.

In Fig. 9, we study the effect of the size of the box L in which the micro simulation is performed for fixed diffuse interface width ε and mobility m. Since we compute in non-dimensional units according to Sec. 2.2 with fixed box height L of unit size, this corresponds to simultaneously changing Cn and S in the computation. In Fig. 9, we express the change in size by comparing results for different box heights L^* compared to the base setting with $\mathrm{Cn} = 0.06$ and $S = 0.0315$. Because of the assumption of a far field behavior according to the similarity solution by Huh and Scriven [24] (see Sec. 2.3), the finite size of the micro box introduces a perturbation of the solution. We observe a close agreement between the solutions for $L = 1$ and $L = 1.33$, especially in the region between 120 and 140 degrees. In the simulations presented in Sec. 4, the apparent contact angle resides mostly in that region, which promises accurate results. The relation between θ_a and U in this region is approximately linear. A linear relation was used e.g. by Spelt [41]. The results indicate that the box size is sufficiently large for $S = 0.0315$.

3 Macro model

For the macro model, we develop a level set discretization with sharp treatment of the interface forces with the ghost fluid method. The contact point is tracked explicitly using the tabulated contact point velocities form the micro model. To avoid the singular stresses in the momentum equation, a Navier condition with a non-zero slip length only around the contact point is imposed for the wall parallel component of the momentum equation.

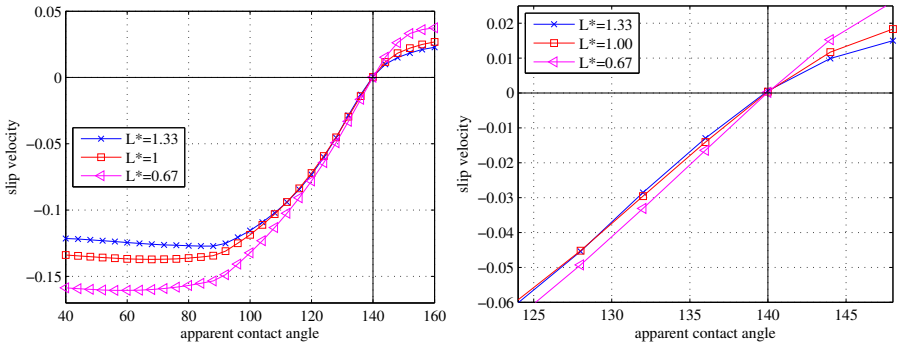

(a) Full range of contact angles. (b) Zoom around static contact angle.

Figure 9: Wall velocities for oil/water material combination for different sizes of the simulation domain L^*. The material parameters are constant $\mathrm{Cn} = 0.06$ and $S = 0.0315$. The mesh size is kept constant at $h = L^*/64$ and the time step at $\Delta t = 0.005$.

3.1 Bulk model

For a sharp interface method, the incompressible Navier–Stokes equations (4)–(5) for each fluid can be simplified by dropping surface tension and using the standard Laplacian for diffusion,

$$\nabla \cdot \mathbf{u} = 0, \tag{14}$$

$$\rho \left(\frac{\partial \mathbf{u}}{\partial t} + (\mathbf{u} \cdot \nabla)\,\mathbf{u} \right) = -\nabla p + \mu \nabla^2 \mathbf{u} + \rho \mathbf{g}. \tag{15}$$

These equations are augmented by jump conditions at the interface between the two fluids, see Sec. 3.2 below. In general, the material properties μ and ρ are different for the two fluids.

The discretization is done on a uniform staggered grid, where the scalar quantities, i.e., pressure p, are stored at the cell centers while the velocity components u and v are stored at the vertical and horizontal cell faces, respectively [19]. The advection terms in the momentum equation (15) are discretized by a 5th order Hamilton–Jacobi WENO scheme [12], because the WENO scheme can handle the discontinuities in the first derivative of the velocity without further modification. At points which are not adjacent to the interface, the viscous terms are discretized by second order central difference stencils. To enforce the incompressibility, a direct projection (non-incremental pressure correction) is applied [15]. First an intermediate velocity $\mathbf{u}^*$ is obtained by updating the velocity from the previous time step with the advective, viscous and gravity terms,

$$\mathbf{u}^* = \mathbf{u} + \Delta t \left(-(\mathbf{u} \cdot \nabla)\,\mathbf{u} + \frac{\mu}{\rho} \nabla^2 \mathbf{u} + \mathbf{g} \right). \tag{16}$$

This intermediate velocity field is then used to determine the right hand side of the Poisson equation for the scaled pressure correction $p^* = p/\Delta t$. At walls homogeneous Neumann boundary conditions are applied to solve for p^*,

$$\nabla \cdot \left(\frac{\nabla p^*}{\rho} \right) = \nabla \cdot \mathbf{u}^*. \tag{17}$$

Away from the interfaces, the density ρ corresponds to the constant density of the fluid at this location, so the Laplace operator is approximated by the standard second order 5 point central finite difference stencil. Finally, the intermediate velocity is made divergence free by using the solution of the Poisson equation (17) for the pressure correction,

$$\mathbf{u}^{n+1} = \mathbf{u}^* - \frac{\nabla p^*}{\rho}. \tag{18}$$

This projection procedure can be viewed as a special time splitting scheme which is advancing the solution Δt in time like one time step in a forward Euler scheme. Therefore, a repetition of the projection procedure can be employed to form a Runge-Kutta time integration scheme. In the present work, the 3rd order TVD Runge-Kutta method by Shu and Osher [40] is applied. An expression for the maximum allowed time step for a forward Euler time integration considering advection, diffusion, surface tension, and gravity is given by Kang et al. [27].

3.2 Interface conditions

Since we use the ghost fluid method (GFM) [29], conditions at the interface are accounted for by a modification of the finite difference stencils. This obviates a source term for surface tension like in equation (5) in the momentum equation. The boundary conditions at the interface can be derived by considering an infinitesimal control volume across the interface. For the case with constant surface tension σ and no mass transfer across the interface, we get the following jump conditions,

$$[\![\mathbf{u}]\!] = 0, \tag{19}$$

$$\left[\!\!\left[\begin{pmatrix} \mathbf{n}^T \\ \mathbf{t}^T \end{pmatrix} (p\mathbf{I} - \tau)\,\mathbf{n} \right]\!\!\right] = \begin{pmatrix} \sigma\kappa \\ 0 \end{pmatrix}, \tag{20}$$

where square brackets define the jump across the interface, e.g. $[\![\mathbf{u}]\!] = \mathbf{u}_1 - \mathbf{u}_2$. The subscripts are used to denote the values on the two sides of the interface. We further denote by $\mathbf{n}$ and $\mathbf{t}$ the unit normal and tangent vectors to the interface. The parameter κ is the local interface curvature and $\tau = \mu\nabla^s\mathbf{u}$ is the viscous stress tensor. These conditions imply that the velocity and tangential stresses are continuous across the interface, whereas the normal stresses are discontinuous.

The jump conditions at the interface (20) can be rewritten such that jumps are separated for the derivatives of the velocity components [27]. Those separated jump conditions together with the GFM allow to treat the jumps in a sharp manner. If there is an interface crossing the grid lines of a stencil, the known jumps are added or subtracted from the points on the opposite side of the interface. This addition or subtraction is then included into the second order finite difference method. The treatment of the jump condition is improved by interpolating the jump condition to the position where the interface intersects the grid lines. More details on the implementation of the GFM for two phase flow can be found in the references [27, 29].

The level set method (LSM) [39] is used to keep track of the interface position. The interface is defined as the zero contour line of a signed distance function ϕ. The signed distance function is advected with the local fluid velocity using the advection

equation

$$\frac{\partial \phi}{\partial t} + \mathbf{u} \cdot \nabla \phi = 0. \tag{21}$$

Since ϕ loses its signed distance property over time, it has to be reinitialized by solving the reinitialization equation

$$\frac{\partial \phi}{\partial \tau} + \operatorname{sign}(\phi)\,(|\nabla \phi| - 1) = 0 \tag{22}$$

with respect to the pseudo time τ. The interface normal and curvature can be obtained directly from the signed distance function,

$$\mathbf{n} = \frac{\nabla \phi}{|\nabla \phi|}, \tag{23}$$

$$\kappa = -\nabla \cdot \mathbf{n}. \tag{24}$$

The same 5th order Hamilton–Jacobi WENO scheme as in the advection terms of the momentum equations (15) is used to discretize the LSM advection and reinitialization equations. To minimize spurious displacements of the interface during the reinitialization, the constrained reinitialization CR-1 [20] is applied. The normals and curvature are computed by standard second order finite difference stencils.

3.3 Contact point

The contact point is tracked explicitly by the ordinary differential equation

$$\frac{\mathrm{d}x_{\mathrm{CP}}}{\mathrm{d}t} = f(\theta_a), \tag{25}$$

where θ_a is the apparent contact angle measured in the macro model and f is the function obtained form the micro model. The contact point position is updated by a forward Euler step directly after the advection of the level set function ϕ. There is a direct coupling between the contact point position and the flow field trough the curvature computation described below. The movement of the contact point will cause a change in the curvature and hence the pressure jumps at the wall. For example in the capillary driven channel flow Sec. 4.1, if the contact point moves faster to the right than the interface in the bulk, the curvature at the wall as well as the jump in the pressure will increase. This causes a higher fluid velocity at the first grid point. It can be seen from the results that through this coupling the velocity at the first grid point matches the contact point velocity as the interface is traveling to the right.

The curvature κ and the contact angle cannot be computed with central differences at the wall since the stencil for the first grid point in the fluid would contain points outside the computational domain. As discussed in more detail below, the interface is assumed to continue as a straight line into the wall and the level set values at the ghost points are set as signed distances to that line. As a result, the curvature at the first grid point would be compromised if computed by central differences. Instead, a circle is fitted through the contact point x_{CP} and the intersection points of the interface with the first two grid lines parallel to the wall. To get convergent curvatures, the intersection points of the grid lines and the zero level set contour are determined by a

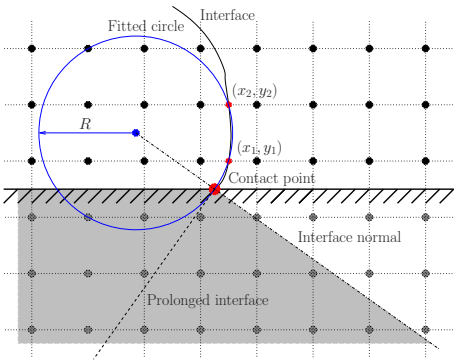

Figure 10: Illustration of the contact point treatment, in the shaded region the ghost points are filled with the analytical distance to the interface if this is smaller than the value of ϕ extrapolated perpendicular to the wall.

cubic interpolation. The curvature at the first grid point is then given as the inverse of the radius R from the fitted circle. The smaller angle between the wall and the fitted circle is

$$\hat{\theta} = \sin^{-1}\left(\frac{|x_{\mathrm{CP}} - x_m|}{R}\right), \tag{26}$$

where x_m is the x-position of the center from the fitted circle, cf. Fig. 10. Using the y-position of the circle center and the sign of the first grid point left of the interface, it can be checked whether $\hat{\theta}$ is the contact angle in the desired fluid and we set $\theta_a = \hat{\theta}$. Otherwise the correct angle is obtained by $\theta_a = \pi - \hat{\theta}$. The choice to fit a circle as opposed to e.g. a second order polynomial is justified by the fact that the interface on the macro scale will assume a circular shape at steady state. During the reinitialization, the interface suffers from spurious displacements. Therefore, the reinitialization will change the measured contact angle and curvature, since they depend on the first two interpolated intersection points. The spurious displacement and therefore the change of the contact angle and curvature are efficiently reduced by the constrained reinitialization.

Since we track the contact point independently of the level set function, care has to be taken to ensure that the zero contour line of ϕ actually crosses the contact point. This can be achieved by a proper choice of boundary conditions during the reinitialization of ϕ. The LSM reinitialization equation can be rewritten as a hyperbolic equation where the characteristics are perpendicular to the interface [37]. Therefore, the position of the interface decides where a boundary condition for the reinitialization is required. In areas where no boundary condition is required, the values in the ghost points for the signed distance function are computed by a linear extrapolation perpendicular to the wall. To fill the ghost points in areas where a boundary condition is required, the interface is prolonged as a straight line from the contact point with a slope given by θ_a. The regions where a boundary condition is necessary are located close to the contact point. Since the interface crosses the wall at the contact point, there will be characteristics pointing from the wall into the fluid on one side of the interface. For all ghost points which are below a line which is perpendicular to the interface at the contact point (shaded area in Figure 10), the distance to the prolonged

interface is computed analytically. In addition, the sign of the distance can be deduced from the first fluid point adjacent to the interface. To ensure that the reinitialization solution obeys the characteristics, the ghost points are finally filled, either with the perpendicularly extrapolated value, or the distance to the prolonged interface, depending on which of the two has the smaller absolute value. If there are multiple contact points, the interface is only prolonged until it reaches the x-position of the neighbouring ghost point. Then, the distance to the closest prolonged interface is selected.

3.4 Boundary condition for the momentum equation

A boundary condition for the momentum equation parallel to the wall is necessary. This boundary condition should account for the slip between the wall and the contact point. Otherwise the stresses would become singular around the contact point. To avoid this singularity, a number of authors used a Navier condition (1) parallel to the wall with a slip length λ constant along the entire wall. The discrete no-slip boundary condition on a staggered grid corresponds to a Navier slip boundary condition with $\lambda = O(\Delta x^2)$ due to the interpolation error.

A different approach is to set the velocity in the proximity of the contact point equal to the contact point velocity itself and to let it smoothly approach the wall velocity as the distance to the contact point increases. The length scale L_s of this smooth transition is of the order of the diffusion length scale S. This approach was followed by Dussan [7]. It was shown that the results for different velocity profiles only differ within a region of the extend of the order of L_s. Our preliminary numerical experiments reveal that a given wall velocity profile or a slip boundary condition with a non-zero λ close to the contact point will produce results which are similar away form the contact point, as long as the length scale L_s is kept constant.

Both length scales λ and L_s are too small to be properly represented by the macro model. Here we adopt a combination of the two approaches mentioned above. Instead of prescribing a velocity boundary condition, we use equation (1) with a slip length which is non-zero only in the vicinity of the contact point. Since almost complete slip is required around the contact point, the grid points directly to the right and left of the contact point have a large slip length which is reduced to zero over the next three grid points. In the following, the slip length is set to $\lambda = 100$ for the grid points adjacent to the contact point and is then reduced to $\lambda = 1$ and 0.01 over the two consecutive grid points.

In Sec. 4.1, we show that this boundary condition leads to converging results. In Table 2, we present a result where λ has been multiplied by 10. The increase of λ causes a much smaller change in the result than doubling of the amount of grid points. Therefore it is assumed that the used values of λ allow enough slip around the contact point.

4 Computational results

In this section, we present computations of two flows dominated by capillary forces, a capillary driven channel flow and an advancing droplet.

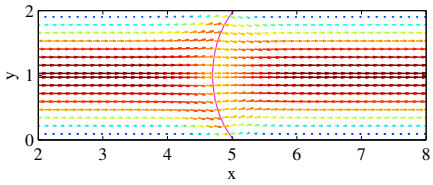

Figure 11: Velocity field and interface position for capillary driven channel flow as the contact point passes $x = 5$.

4.1 Capillary driven channel flow

To test the boundary condition for the momentum equation, we compute a capillary rise in a horizontal channel. In the following, we use non-dimensional variables. Two immiscible fluids are placed between two plates separated by a distance of 2. The length of the channel is 10 and the pressure is fixed to zero at the in- and outlet. There is no gravity acting on the fluids. Initially the interface between the two fluids is a straight line at $x = 3.5$. After an initial transient, the interface assumes a curved shape and travels with an almost constant velocity towards the right as the viscous and capillary forces are in balance. The mass densities of the two fluids are $\rho_1 = 1$ and $\rho_2 = 0.8$ and the dynamic viscosities are $\mu_1 = 0.3$ and $\mu_2 = 1$, respectively. The viscosity ratio corresponds to the value for water and oil as discussed in Sec. 2.5. The surface tension between the fluids is $\sigma = 1$ and the static contact angle, measured in fluid 2, is $\theta_s = 140^\circ$. The fluid labeled 1 is located to the left of the interface.

The velocity field and the interface position at a time after the inital transient are displayed in Fig. 11. In Fig. 12, the contact point velocity and position are plotted for a number of increasingly refined grids. The results are converging as the grid is refined. The slow increase of the contact point velocity after the transient is due to the reduction of the overall viscous force as the less viscous fluid displaces the one with higher viscosity. The contact point velocity is oscillating considerably at lower resolution. As the resolution is increased, the amplitude of the oscillations is reduced while their frequency increases. The cause for the oscillations is the interpolation of the intersection point between the zero level set of ϕ and the grid lines which are used to compute the curvature at the contact point as well as the contact angle. The interpolation errors depend on the distance between the intersection point and the next grid points. Consequently, the estimation of the contact angle changes as the interface is moving relative to the grid. With an increasing grid resolution, the errors in the contact angle approximation decrease and hence the oscillations in the contact point velocity are reduced.

To assess the results obtained with the multiscale method, we compare with results from a plain phase field method (cf. Sec. 2.1). The averaged contact line velocities computed by the two methods are listed in Table 2. The averaging is done over the time interval when the contact point is located between $x = 4.5$ and $x = 5.5$, i.e., after the initial transient. We observe that the averaged velocities computed by the two different models are in qualitative agreement. Note that the average velocity obtained by the phase field method depends on the diffusion length S. For the grid resolutions considered here, the parameter S needs to be chosen larger than a physically meaning-

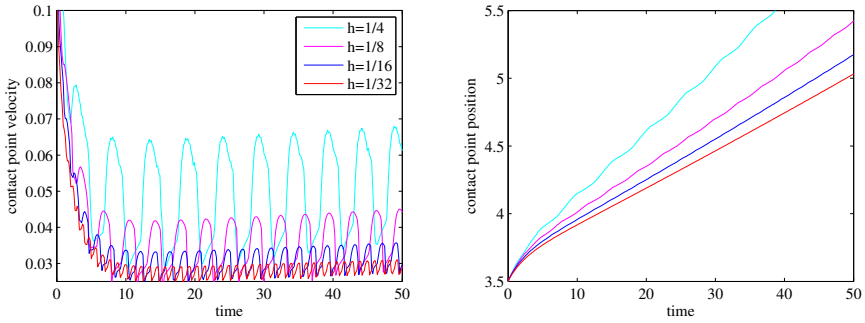

Figure 12: Contact point velocity (left) and position (right) for capillary rise with refined grid.

Table 2: Averaged velocity of the contact point $\bar{v}_{\mathrm{CP}}$ for different grid spacings h for the present multiscale method (left) and pure phase field method (right). The averaging is done over time t when $4.5 \leq x_{\mathrm{CP}}(t) \leq 5.5$. The multiscale result marked with the star was computed using a 10 times larger value of λ around the contact point.

multiscale		phase field		
h	$\bar{v}_{\mathrm{CP}}$	h	S	$\bar{v}_{\mathrm{CP}}$
1/4	0.0499	1/16	0.1	0.0348
1/8	0.0362	1/32	0.1	0.0351
1/16	0.0317	1/16	0.0316	0.0304
1/32	0.0291	1/32	0.0316	0.0309
1/16*	0.0321	1/32	0.0158	0.0283
		1/64	0.01	0.0273

ful value. Consequently, the phase field results do not converge as the diffusion length S is reduced. On the other hand, the results of our multiscale approach are clearly converging as the mesh is refined.

Furthermore, we compare the transient behavior of the two methods in Fig. 13. To this end, we selected a phase field result with similar average velocity as the multiscale result at the highest resolution. We see that our multiscale approach captures the initial transient well and behaves similarly as the phase field approach.

4.2 Advancing droplet

We consider the same fluids as in the previous example. Initially a droplet of the positive fluid is placed on a flat surface. The initial interface shape is a semicircle with a radius of $R_0 = 1$ and a corresponding apparent contact angle of $\theta_a = 90°$. The two contact points are located at $x_{\mathrm{CP}} = \pm 1$. In order to minimize the surface energy, the drop will spread on the surface until the static contact angle is reached. In the final steady state, the interface will assume a circular shape with a radius of $R = \sqrt{\frac{\pi}{2(\pi-\theta_s)-\sin(2(\pi-\theta_s))}}$ and contact point positions $x_{\mathrm{CP}} = \pm R\sin(\pi-\theta_s)$. The velocities are zero at steady state. Because of symmetry, only half of the droplet is computed on a rectangular computational domain of $[0, 2.25] \times [0, 1.5]$, with circle center at the

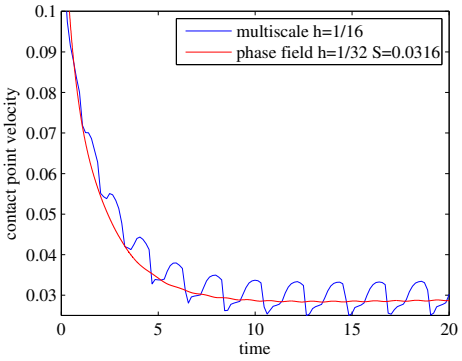

Figure 13: Comparison of the transient evolution of the contact point velocity between the present multiscale method and pure phase field method.

origin. At $x = 0$, $x = 2.25$, and $y = 1.5$ symmetry boundary conditions are applied while at $y = 0$, the wall boundary condition described in Sec. 3.4 is imposed.

The evolution of the interface position as the droplet is spreading and the instantaneous velocity field at $t = 8$ are shown in Fig. 14. As the contact point advances towards the right, a vortex develops. The maximum absolute value of the velocity is always located around the contact point and the slip allowed by the boundary condition is clearly visible. The relatively small capillary number $\mathrm{Ca} = \frac{\mu_2 U_{\mathrm{CP}}}{\sigma} \ll 1$ indicates that the capillary forces are dominating, and hence the interface shape resembles a circle. The deviation from a circular shape is more pronounced at initial times. This is because the large initial difference between the apparent contact angle and the static contact angle leads to a higher contact point velocity U_{CP}. The temporal evolution of the contact point position is displayed in Fig. 15. As before, grid refinement leads to a decrease of the contact point velocity. The mass loss of the level set method [39] is an important contribution to the error in the contact point position at steady state. Since the droplet loses mass over time, the contact point will reach a steady state position which is on the left of the analytically suggested value. It is also slowly receding further as the droplet continues to lose mass. This is clearly visible for the case with the coarse grid spacing $h = 1/8$.

On the basis of energy considerations, Ren et al. [35] derived a scaling law for the contact point position x_{CP} of a small advancing droplet. Their results show that $x_{\mathrm{CP}}(t) \sim t^{\alpha}$, where α is between $1/7$ and $1/5$ depending on whether the viscous forces in the fluids or the friction forces at one of the interfaces dominates the energy dissipation. The right plot in Fig. 15 shows the evolution of contact point position in a logarithmic scale. During the time interval $4 < t < 20$, the contact point position follows the scaling law by Ren et al. [35]. By a least square fit, α is identified as $1/7.0580$, $1/6.8015$, and $1/6.6959$ for grid spacings of $h = 1/8$, $h = 1/16$, and $h = 1/32$, respectively, which agrees well with the theoretical results.

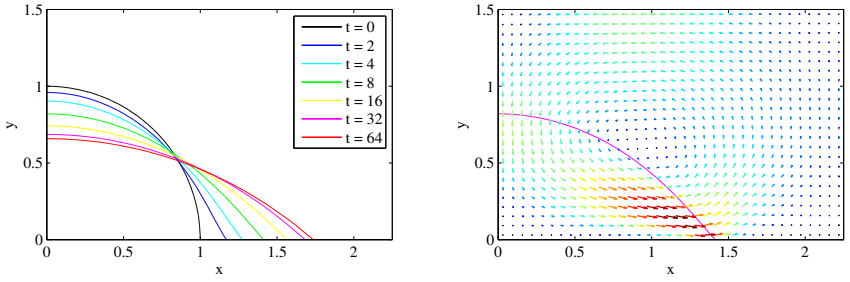

Figure 14: Interface position of the advancing droplet at different times t (left). Interface position and instantaneous velocity field at $t = 8$ (right).

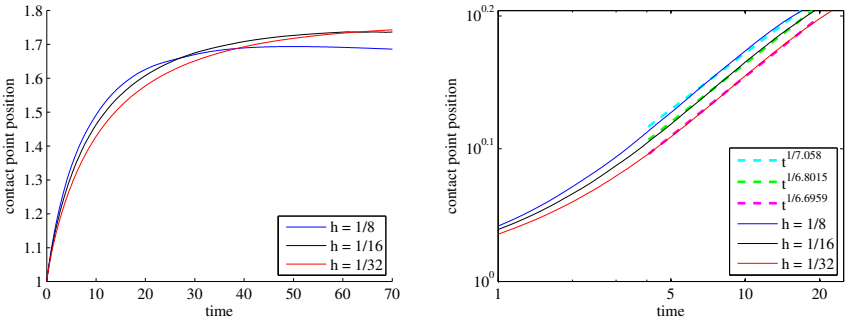

Figure 15: Contact point position of the advancing droplet in linear (left) and logarithmic scales (right).

5 Conclusions

We presented a multiscale method for the simulation of the flow of two immiscible incompressible fluids with moving contact lines. The system was represented by a macro model where the contact point is tracked explicitly and the contact point velocity depends on the apparent contact angle. The relation between this slip velocity and the apparent contact angle was found by a micro model, based on the response of the flow to the molecular forces induced by the macroscopic contact angle. The dimensions of the micro simulation correspond to physical length scales over which contact line diffusion occurs, which makes the results from the phase field micro model represent real material behavior. The micro model was used to tabulate the relation between the contact point velocity and the apparent contact angle for a given material combination. This tabulated data obviates ad-hoc approaches that have previously been used for prescribing the contact point behavior. We presented numerical examples that demonstrate the viability of the approach. A comparison with phase field results shows that our method is able to represent both transient and steady state behavior in

a capillary rise. We also demonstrated agreement of the results with previous studies of advancing droplets.

In our approach, the physical diffusion processes around the contact point which require a highly resolved phase field simulation are incorporated into conventional macro scale techniques like the level set method. We have demonstrated that the effective slip velocity gives a good representation of the physical processes. Therefore, our multiscale method circumvents the necessity to resolve the physical processes at a detailed scale in the macro model by solving a relatively small microscale model. As a result, considerably coarser meshes can be used for the macro scale simulations than for comparable global phase field simulations, which can give tremendous improvements in computational efficiency.

In this study, we have only considered flows driven by capillary forces with a clear separation between the scales of contact behavior and global fluid flow. In future studies, it will be necessary to analyze the given method for flows where the capillary effect is small.

Acknowledgments

Some computations were performed on resources provided by SNIC through Uppsala Multidisciplinary Center for Advanced Computational Science (UPPMAX) under Project
p2010002. M. Kronbichler was supported by the Graduate School in Mathematics and Computing (FMB).

References

[1] W. Bangerth, R. Hartmann, and G. Kanschat. deal.II — a General Purpose Object Oriented Finite Element Library. *ACM Trans. Math. Softw.*, 33(4):article no. 24, 2007.

[2] A. J. Briant and J. M. Yeomans. Lattice Boltzmann simulations of contact line motion. II. Binary fluids. *Phys. Rev. E*, 69:031603, 2004.

[3] J. W. Cahn and J. E. Hilliard. Free Energy of a Nonuniform System. I. Interfacial Free Energy. *J. Chem. Phys.*, 28(2):258–267, 1958.

[4] D. Caviezel, C. Narayanan, and D. Lakehal. Adherence and bouncing of liquid droplets impacting on dry surfaces. *Microfluidics & Nanofluidics*, 5:469–478, 2008.

[5] S. H. Davis. Interfacial fluid dynamics. In G. K. Batchelor, H. K. Moffatt, and M. G. Worster, editors, *Perspectives in Fluid Dynamics*, pages 1–52. Cambridge University Press, Cambridge, 2002.

[6] T. A. Davis. Algorithm 832: UMFPACK V4.3—an unsymmetric-pattern multifrontal method. *ACM Trans. Math. Softw.*, 30:196–199, 2004.

[7] E. B. Dussan V. The moving contact line: the slip boundary condition. *J. Fluid Mech.*, 77(04):665–684, 1976.

[8] W. E and B. Engquist. The Heterogeneous Multiscale Method. *Comm. Math. Sci.*, 1(1):87–132, 2003.

[9] W. E, B. Engquist, X. Li, W. Ren, and E. Vanden-Eijnden. The Heterogeneous Multiscale Method: A Review. *Comm. Comput. Phys.*, 2(3):367–450, 2007.

[10] H. Elman, D. Silvester, and A. Wathen. *Finite Elements and Fast Iterative Solvers with Applications in Incompressible Fluid Dynamics*. Oxford Science Publications, Oxford, 2005.

[11] D. J. Eyre. An Unconditionally Stable One-Step Scheme for Gradient Systems, June 1998, unpublished.

[12] R. P. Fedkiw, T. Aslam, B. Merriman, and S. Osher. A non-oscillatory Eulerian approach to interfaces in multimaterial flows (the ghost fluid method). *J. Comput. Phys.*, 152(2):457–492, 1999.

[13] C. Galusinski and P. Vigneaux. On stability condition for bifluid flows with surface tension: Application to microfluidics. *J. Comput. Phys.*, 227:6140–6164, 2008.

[14] P. M. Gresho and R. L. Sani. *Incompressible Flow and the Finite Element Method*, volume two: Isothermal Laminar Flow. John Wiley & Sons, Chichester, 2000.

[15] J. L. Guermond, P. Minev, and J. Shen. An overview of projection methods for incompressible flows. *Comput. Meth. Appl. Mech. Engrg.*, 195:6011–6045, 2006.

[16] P. R. Gunjal, V. V. Ranade, and R. V. Chaudhari. Dynamics of drop impact on solid surface: Experiments and VOF simulations. *AIChE Journal*, 51(1):59–78, 2005.

[17] N. G. Hadjiconstantinou. *Hybrid atomistic-continuum formulations and the moving contact line problem*. PhD thesis, Massachusetts Institute of Technology. Dept. of Mechanical Engineering, 1998.

[18] E. Hairer, S. P. Nørsett, and G. Wanner. *Solving Ordinary Differential Equations I. Nonstiff Problems*. Springer-Verlag, Berlin, 2nd edition, 1993.

[19] F. H. Harlow and J. E. Welch. Numerical calculation of time-dependent viscous incompressible flow of fluid with free surface. *Phys. Fluids*, 8(8):2182, 1965.

[20] D. Hartmann, M. Meinke, and W. Schröder. The constrained reinitialization equation for level set methods. *J. Comput. Phys.*, 229(5):1514–1535, 2010.

[21] M. Hinze, R. Pinnau, M. Ulbrich, and S. Ulbrich. *Optimization with PDE Constraints*, volume 23 of *Mathematical Modelling: Theory and Applications*. Springer-Verlag, Berlin, 2009.

[22] C. W. Hirt and B. D. Nichols. Volume of fluid (VOF) method for the dynamics of free boundaries. *J. Comput. Phys.*, 39(1):201–225, 1981.

[23] L. M. Hocking. A moving fluid interface. Part 2. The removal of the force singularity by a slip flow. *J. Fluid Mech.*, 79(2):209–229, 1977.

[24] C. Huh and L. E. Scriven. Hydrodynamic Model of Steady Movement of a Solid/Liquid/Fluid Contact Line. *J. Colloid Interf. Sci.*, 35(1):85–101, 1971.

[25] D. Jacqmin. Calculation of two-phase Navier–Stokes flows using phase-field modeling. *J. Comput. Phys.*, 155(1):96–127, 1999.

[26] D. Jacqmin. Contact-line dynamics of a diffuse fluid interface. *J. Fluid Mech.*, 402:57–88, 2000.

[27] M. Kang, R. P. Fedkiw, and X.-D. Liu. A Boundary Condition Capturing Method for Multiphase Incompressible Flow. *J. Sci. Comput.*, 15(3):323–360, 2000.

[28] H. Liu, S. Krishnan, S. Marella, and H. Udaykumar. Sharp interface Cartesian grid method II: A technique for simulating droplet interactions with surfaces of arbitrary shape. *J. Comput. Phys.*, 210:32–54, 2005.

[29] X.-D. Liu, R. P. Fedkiw, and M. Kang. A Boundary Condition Capturing Method for Poisson's Equation on Irregular Domains. *J. Comput. Phys.*, 160(1):151–178, 2000.

[30] T. Qian, X.-P. Wang, and P. Sheng. Molecular scale contact line hydrodynamics of immiscible flows. *Phys. Rev. E*, 68:016306, 2003.

[31] T. Qian, X.-P. Wang, and P. Sheng. Power-Law Slip Profile of the Moving Contact Line in Two-Phase Immiscible Flows. *Phys. Rev. Lett.*, 93:094501, 2004.

[32] T. Qian, X.-P. Wang, and P. Sheng. Molecular Hydrodynamics of the Moving Contact Line in Two-Phase Immiscible Flows. *Comm. Comput. Phys.*, 1(1):1–52, 2006.

[33] W. Ren and W. E. Heterogeneous multiscale method for the modeling of complex fluids and micro-fluidics. *J. Comput. Phys.*, 204(1):1–26, 2005.

[34] W. Ren and W. E. Boundary conditions for the moving contact line problem. *Phys. Fluids*, 19:022101, 2007.

[35] W. Ren, D. Hu, and W. E. Continuum model for the moving contact line problem. *Phys. Fluids*, 22:102103, 2010.

[36] M. Renardy, Y. Renardy, and J. Li. Numerical simulation of moving contact line problems using a volume-of-fluid method. *J. Comput. Phys.*, 171:243–263, 2001.

[37] G. Russo and P. Smereka. A remark on computing distance functions. *J. Comput. Phys.*, 163(1):51–67, 2000.

[38] P. Seppecher. Moving contact lines in the Cahn–Hilliard theory. *Int. J. Engng. Sci.*, 34(9):977–992, 1996.

[39] J. A. Sethian and P. Smereka. Level Set Methods for Fluid Interfaces. *Ann. Rev. Fluid Mech.*, 35(1):341–372, 2003.

[40] C.-W. Shu and S. Osher. Efficient implementation of essentially non-oscillatory shock-capturing schemes. *J. Comput. Phys.*, 77(2):439–471, 1988.

[41] P. D. M. Spelt. A level-set approach for simulations of flows with multiple moving contact lines with hysteresis. *J. Comput. Phys.*, 207:389–404, 2005.

[42] P. Yue, C. Zhou, and J. J. Feng. Sharp-interface limit of the Cahn–Hilliard model for moving contact lines. *J. Fluid Mech.*, 645:279–294, 2010.

[43] S. Zahedi, G. Kreiss, and K. Gustavsson. A conservative level set method for contact line dynamics. *J. Comput. Phys.*, 228:6361–6375, 2009.